Epitaxial superlattices as a framework for stabilizing different LaNiO₃ structures

F. Misják [1,2,*] R. A. Ortiz [2,3] D. Geiger,[1] M. K. Kinyanjui,[1] E. Schierle,[4] K. Fürsich [3] G. Christiani,[3] G. Logvenov,[3]
B. Keimer,[2,3] U. Kaiser [1,2] and E. Benckiser [3,2,†]

[1]*Central Facility of Electron Microscopy and Institute for Quantum Optics, Ulm University, Albert-Einstein-Allee 11, 89081 Ulm, Germany*
[2]*Center for Integrated Quantum Science and Technology (IQST), 70569 Stuttgart, Germany*
[3]*Max Planck Institute for Solid State Research, Heisenbergstraße 1, 70569 Stuttgart, Germany*
[4]*Helmholtz-Zentrum Berlin für Materialien und Energie, Albert-Einstein-Straße 15, 12489 Berlin, Germany*

Targeted material design is at the center of research efforts on epitaxial, complex oxide heterostructures. Due to the strong electron-lattice coupling, small structural modifications are often decisive for the resulting macroscopic, physical properties of artificially layered materials. Here we report on a detailed structural analysis of a set of differently stacked LaNiO₃-LaGaO₃ superlattices by transmission electron microscopy. We find that the relative thickness ratio of the two superlattice sublayers affects the structural network, resulting in different Ni–O bond lengths and Ni–O–Ni angles under the same epitaxial strain conditions. Whereas the bond length values depend mainly on the LaNiO₃ layer thickness, bond angles are mainly influenced by the LaGaO₃ layer thickness. The orbital polarization determined from x-ray absorption spectroscopy measurements shows that the superlattice with the smallest deviation of both values compared to bulk shows the highest orbital polarization. Therefore, the thickness ratio of the two superlattice components can be regarded as an additional effective tool to tune the functional properties of nickelates.

I. INTRODUCTION

The rare-earth nickelates with the composition RNiO₃ (R = rare earth) show a diverse phase diagram [1,2]. All RNiO₃ with $R \neq$ La exhibit a metal-insulator transition (MIT) and complex magnetic ordering at low temperatures. The insulating phase has been explained by a bond disproportionation mechanism that is based on an understanding of nickelates as self-doped negative charge-transfer systems [3,4]. The bond disproportionation then is a breathing distortion of neighboring NiO₆ octahedra into a checkerboard pattern of large and small octahedra in the cubic perovskite structure. The electronic configuration in the small and large octahedra disproportionates towards Ni-$3d^8$ + Ni-$3d^8\underline{L}^2$, leading to localization. Here $\underline{L}$ denotes an oxygen ligand hole. The breathing distortion is linked to the low-temperature monoclinic crystal structure (space group $P2_1/m$, No. 11) with two nonequivalent nickel sites, which is a subgroup of the high-temperature, metallic $Pbnm$ (No. 62) structure [5]. The crystal structure of LaNiO₃ is also an exception in the family, as a rhombohedral space group with only one Ni position $R\bar{3}c$ (No. 167) has been reported for this compound down to

low temperatures [5]. A more recent neutron diffraction study on powder samples showed that at very low temperatures, LaNiO₃ exhibits local monoclinic $P2_1/m$ symmetry, which indicates a close proximity to an insulating state with bond disproportionation, despite its macroscopic metallic behavior [6].

The predisposition of the lattice for this distortion opens the possibility to stabilize various phases in specifically designed heterostructures [7–9]. This motivates the present paper, in which we investigate the crystalline structure of LaNiO₃-LaGaO₃ (LNO-LGO) superlattices (SLs) with varying slab thicknesses between four and eight pseudocubic unit cells (see sketch in the inset of Fig. 1). The second material LGO has a $Pbnm$ structure, and we aim to investigate how these materials with different bulk structures grow on top of each other. Since LGO is a large-gap band insulator, we assume that there is no charge transfer or magnetic interaction between the materials. In LNO-LaAlO₃ SLs, where both constituents have $R\bar{3}c$ structure in bulk, the averaged crystal structure was refined in the space group $I2/c11$ (No. 15), a subgroup of $R\bar{3}c$ [10]. The group-subgroup relationship is reflected in the corresponding Glazer pattern, where the structural differences are reduced to tilts and rotations of rigid octahedra around the cubic perovskite axes. [11]. The Glazer pattern for $R\bar{3}c$ is $a^-a^-a^-$, with equal antiphase rotations around all three axes. For the subgroup $I2/c11$, only the magnitude of the rotation around the c axis changes, and the pattern is $a^-a^-c^-$. Accordingly, the tilt pattern for $Pbnm$ is $a^-a^-c^+$ with a distinct in-phase rotation of octahedra around the c axis. In the $P2_1/m$ subgroup structure, this pattern changes to $a^-b^-c^+$ with a change of magnitude of rotations around b. Most importantly the two low-symmetry subgroup structures are different with respect to their Ni positions.

---

*fanni.misjak@alumni.uni-ulm.de
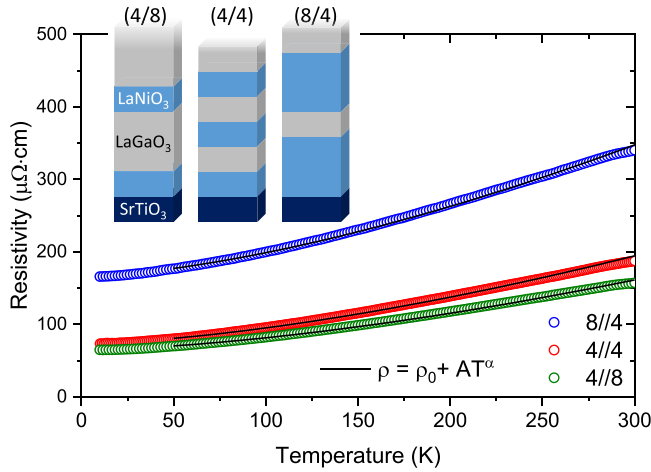†E.Benckiser@fkf.mpg.de

FIG. 1. Resistivity of LNO-LGO SLs with three different stacking sequences as sketched in the inset. The following values for the total thickness of the LNO sublayers in the different structures used to calculate the resistivity were $D_{8/4} = 317 \pm 15$, $D_{4/4} = 122 \pm 2$, and $D_{4/8} = 111 \pm 10$ Å. To fit the temperature-dependent resistivity (black lines), the value of residual resistivity has been fixed to the resistivity value at $T = 10$ K: $\rho_0^{8/4} = 165.9$, $\rho_0^{4/4} = 73.4$, and $\rho_0^{4/8} = 64.7$ $\mu\Omega$cm.

While $P2_1/m$ has two Ni positions, $I2/c11$ does not, implying that a bond-disproportionated ground state is not possible, at least not from an average, macroscopic crystal symmetry point of view.

Given the two different Glazer patterns favored by bulk LNO and LGO, the question is whether they are preserved in the SL sublayers of the components under the biaxial strain from the substrate and, if so, how they are connected across the interfaces. At such heterointerfaces, where two materials with different cations and crystal symmetries are coherently stacked, the octahedral network must rearrange to maintain connectivity. This results in changes in bond lengths and bond angles with a direct effect on the physical properties [9,12]. The substitution of rare-earth ions in nickelates leads to an increase in the MIT temperature with decreasing rare-earth ion radius from Nd to Lu [1]. This is driven by an increasing deviation of the Ni–O–Ni bond angle from $180°$. Changing the Ni–O–Ni bond angle in turn changes the bandwidth, i.e., the smaller the angle, the narrower the bandwidth and the larger the band gap. In epitaxial heterostructures, the relative thickness ratio of the different layers can influence the structure in a similar way [13–18]. Recently, Chen *et al.* reported a non-monotonic dependence between the layer thickness and the MIT in tetragonal NdNiO$_3$/SrTiO$_3$ superlattices [16]. While the thickness of the cubic SrTiO$_3$ layers was kept constant at four unit cells, the oxygen octahedral rotations in NdNiO$_3$ were observed to evolve from a modulated to a uniform pattern as their thickness was reduced. These structural changes are related to changes in the MIT and the antiferromagnetic transition.

Here we investigate the structural changes in LNO-LGO superlattices in which different octahedral rotation patterns are already present in the bulk structures of both components. To this end, we determine the structure of the

octahedral network using aberration-corrected high-resolution TEM (AC-HRTEM) to map the layer-resolved octahedral distortions by imaging small oxygen atom displacements in different LNO-LGO SLs with systematically varied stacking sequences. We find a significant variation in the out-of-plane bond lengths and angles that is not simply related to the orbital polarization determined from the linear dichroism in the Ni-$L_{3,2}$ x-ray absorption spectra.

II. EXPERIMENTAL DETAILS

The LNO/LGO (n/m) SLs were grown by pulsed laser deposition on cubic (001) SrTiO$_3$ (STO) substrates with growth parameters reported in Ref. [19]. The growth starts from the substrate with n pseudocubic unit cells of LNO followed by m unit cells of LGO. The (n/m) bilayer structure, where $n = 4, 8$ and $m = 8, 4$ was then repeated eight and ten times, respectively (inset in Fig. 1). Resistance measurements for all three SLs were performed in van der Pauw geometry. We have determined the isotropic resistivity $\rho_{\rm iso}$, shown in Fig. 1, from the four-probe measurement of the resistances with reversed current and voltage contact pairs using the equations derived in Ref. [20]. The sample thickness enters the equation, as it relates the sheet resistance to the three-dimensional resistivity. Since LNO is the conductive component of the heterostructure, we used the LNO slab thickness, determined by x-ray reflectometry and multiplied by the number of bilayer layer repetitions to obtain the effective, total nickelate thickness D. All three SL samples show good conductivity with a metallic temperature dependence down to 4 K (Fig. 1).

The electrical resistivity of a metal can be described as the sum of a temperature-independent residual resistivity ρ_0, resulting from static imperfections such as point defects or vacancies, and a temperature-dependent term $\rho(T)$, resulting from the dynamic deviations from crystal perfection. According to the Matthiessen rule, the latter is sample independent. The residual resistances of the 4/4 and 4/8 SLs are comparable to those observed in LNO thin films [21] and LNO-LaAlO$_3$ superlattices [22], while ρ_0 of the 8/4 SL is larger by more than a factor of 2, which may be related to a higher density of oxygen vacancies [23]. To evaluate the temperature dependent term $\rho(T)$, we use the power law

$$\rho = \rho_0 + AT^\alpha, \tag{1}$$

where A is a coefficient related to the strength of electron scattering, and α is the power-law exponent. To determine A and α, we fitted straight lines to $\ln(\rho - \rho_0) = \ln(A) + \alpha \ln(T)$ in the range $T = 50$–300 K (black lines in Fig. 1). For an ordinary metal, one would expect a linear temperature dependence ($\alpha = 1$) of the resistivity in the electron-phonon scattering dominated regime. The values of the SLs deviate from linearity and vary around $\alpha \sim 1.55$, suggesting additional scattering mechanisms. Previous studies on epitaxial thin films have shown that the values of the exponent can be tuned by a combined effect of epitaxial strain, film thickness, and disorder due to oxygen vacancies between 1 and 3 [24]. We will return to the observed differences in the temperature-dependent scattering between the SLs structures, i.e., the dependence of A and α on the thickness ratio of the two superlattice components, in our discussion of Fig. 5.
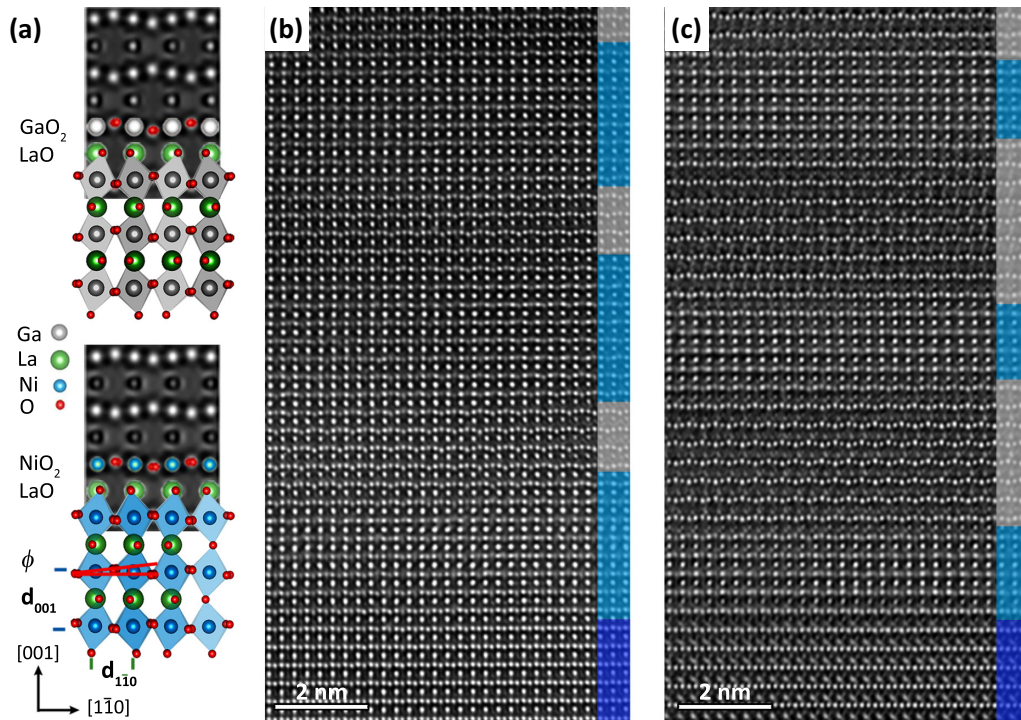
FIG. 2. (a) Simulated $[110]_{pc}$ HRTEM image of bulk LGO and bulk LNO overlaid with the corresponding atomic model; the parameters evaluated in the SLs are also shown. (b) Characteristic 300 kV AC-HRTEM images of the 8/4 and (c) 4/8 sequence of LNO-LGO SLs in $[110]_{pc}$ projection. The images were acquired under negative C_s-imaging conditions ($C_s = -15$ μm) and slight overfocus ($\Delta f \sim +5$ nm). The interfaces between the STO substrate (dark blue) and LNO (blue)-LGO (grey) sublayers are marked. The growth direction of the SLs is parallel to $[001]_{pc}$.

X-ray absorption spectroscopy (XAS) measurements were performed at the UE46 PGM-1 beamline at HZB, BESSY-II, Germany. All XAS measurements were detected in total electron yield mode. The measurements were performed using linearly polarized soft x-rays (σ and π polarization) at incident angles of $\theta = 30°, 45°$. To obtain the spectra with polarization of incoming x-rays $E \parallel [001]$ and $E \perp [001]$, we used the formulas $I_{\perp[001]} = I_\sigma$ and $I_\pi(\theta) = I_{\perp[001]}\cos^2\theta + I_{\parallel[001]}\sin^2\theta$ [25].

The cross-sectional TEM specimens were prepared by a focused ion beam (FIB) technique using NVision 040Ar with an unique X2 holder [26] for high-quality lamella preparation. The FIB-prepared samples were then cleaned using low-voltage Ar ion milling by Fischione Nanomill [27].

AC-HRTEM imaging was performed using an image-side C_s-corrected FEI Titan 80-300 microscope operated at 300 kV. The FEI Titan is equipped with a CEOS hexapole aberration corrector, which allows the correction of the geometrical axial aberrations up to the third order. To identify the octahedral behavior, measurement of oxygen positions in the films is required. Imaging conditions were chosen to optimize the visibility of the oxygen atoms between the heavier $B =$ Ni or Ga atoms in the BO_2 layers [Fig. 2(a)]. For this, AC-HRTEM images were acquired from a sample with a thickness of approximately 10 nm, under negative C_s imaging conditions with spherical aberration coefficient $C_s \sim -15$ μm compensated with slight positive defocus values [28,29].

For quantitative analysis, the AC-HRTEM images were noise filtered by a Wiener filter to enhance the signal. CalAtom [30] and a custom MATLAB code were used to determine the atomic column positions in the $[110]_{pc}$ HRTEM images and to extract the lattice parameter and angle values. To increase the accuracy of the evaluation, the measured values were averaged per each in-plane atomic row shown in the HRTEM images. This means averaging over 30 unit cells (u.c.) of the pseudocubic perovskite lattice layer along the $[1\text{-}10]_{pc}$ direction for each plotted point. The STO substrate was used as internal calibration. The lattice parameter d_{001} and the crystal plane distance $d_{1\text{-}10}$ were measured and represent the distance between the B atoms. In $[110]_{pc}$ projection, the out-of-plane spacing corresponds to the out-of-plane lattice parameter d_{001}, while the in-plane lattice spacing d_{1-10} is related to the in-plane lattice parameters $d_{010} = d_{100}$ through the following equation: $d_{100} = d_{010} = \sqrt{2}d_{1-10}$ [Fig. 2(a)]. The projected tilt angle ϕ of the oxygen octahedra along the $[1\text{-}10]_{pc}$ direction was also determined by averaging over 30 u.c. of the pseudocubic perovskite lattice layer.

III. RESULTS

Quantifying the structural distortions within the Glazer formalism [11], LNO bulk is described by $a^-a^-a^-$, with equal $\alpha = \beta = \gamma = 5.2°$ angles [5] about the pseudocubic [100], [010] and [001] axes, respectively. For bulk LGO with $a^-a^-c^+$ pattern, $\alpha = \beta = 6.17°$ and $\gamma = 5.2°$ have been reported [31]. The pseudocubic (pc) lattice parameters are $a_{LNO,pc} = 3.84$ Å, and $a_{LGO,pc} = 3.89$ Å, respectively. Both SL components, LNO and LGO, are under tensile biaxial strain induced by the cubic STO substrate with $a_{STO} = 3.905$ Å.
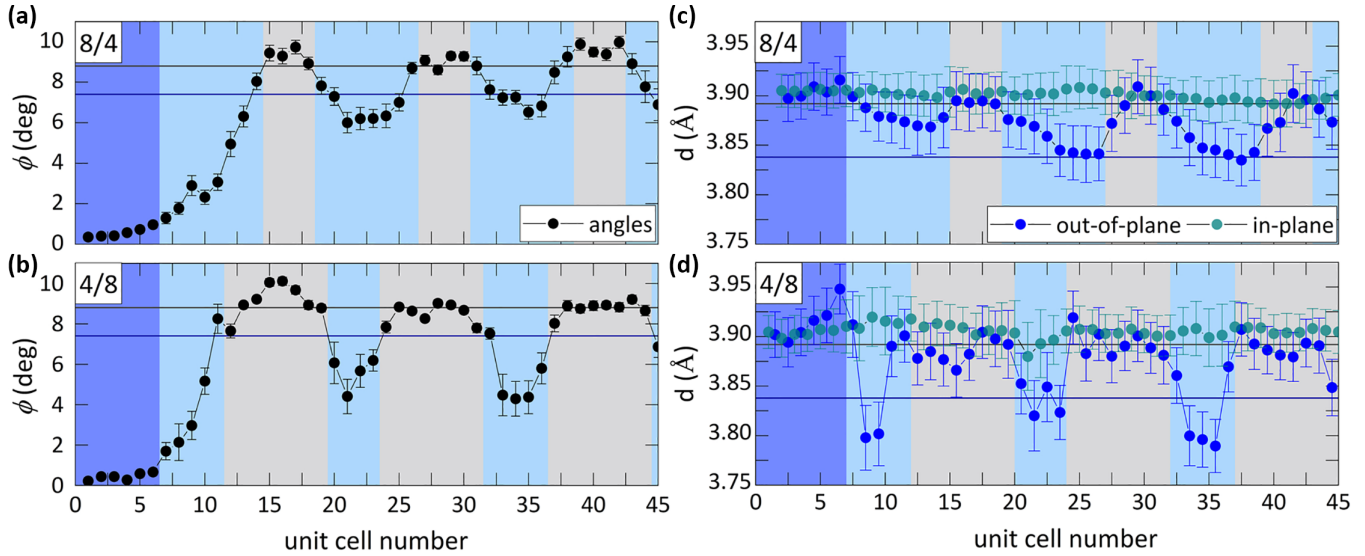
FIG. 3. Quantitative analysis of the 8/4 and 4/8 LNO/LGO SLs on STO substrate. The location of the STO substrate (dark blue) and LNO (light blue), and LGO (gray) sublayers are marked. Values of the (a), (b) ϕ angles (black); (c), (d) out-of-plane d_{001} (blue); and in-plane d_{100} (green) lattice spacing as a function of the location in the respective SL is shown. Each data point represents the average value of 30 u.c. along the $[1\text{-}10]_{pc}$ direction. The error bars correspond to the standard deviation associated with the statistical averaging. The solid horizontal lines represent the corresponding values of bulk LNO (blue - $\phi_{\text{bulk,LNO}} = 7.4°$, $d_{001,\text{bulk,LNO}} = 3.838$ Å) and LGO (gray - $\phi_{\text{bulk,LGO}} = 8.8°$, $d_{001,\text{bulk,LGO}} = 3.892$ Å).

A previous study on LNO thin films, grown on STO substrates, revealed a $a^- a^- c^-$ pattern with a small γ angle [18,32]. Density functional theory calculations showed that LNO films under tensile strain show enhanced α and β tilts, with γ being suppressed already at moderate strain and having an $a^- a^- c^0$ pattern [33]. Since enhanced in-plane octahedral rotations can be most accurately measured in the $[110]_{pc}$ projection (and not in the $[1\text{-}10]_{pc}$ projection) we have chosen this projection in our HRTEM measurements.

Figure 2(a) shows simulated images of LNO and LGO in $[110]_{pc}$ projection under negative C_s image conditions. The atomic columns appear with white atom contrast on a dark background. In the $[110]_{pc}$ projection, the B (B = Ni or Ga) and A (A = La) atoms are separated, and in-between the heavier B cations, the oxygen anions are imaged in white atom contrast. Those represent the projected position of the basal oxygen ions of the octahedra in the horizontal (001) plane. Due to the octahedral rotations, the oxygen positions shift up and down about the horizontal B-B line forming zigzags. The zigzag tilt value relates to the magnitude of octahedral rotations. In the SL framework, the corner-connected octahedral network must rearrange to maintain the oxygen octahedral connectivity at the heterointerfaces between constituents with different octahedral patterns. By following the positions of the oxygen atoms, it is possible to follow the rearrangement of the BO_6 octahedra and to determine the sizes of the rotations about the [100] and [010] axes (α and β). Figures 2(b) and 2(c) show representative AC-HRTEM images of the 8/4 and 4/8 SLs, respectively, across the substrate and SL interfaces. We denote the growth direction of the SLs by $[001]_{pc}$. The structural differences between the $[110]_{pc}$ projection of STO, LNO, and LGO allowed us to distinguish the LNO and LGO sublayer in the HRTEM images as indicated by the colored side bands in Figs. 2(b) and 2(c). The HRTEM images show

well-ordered SL structures and prove that the SLs are coherently strained.

To quantitatively analyze the octahedral tilt patterns across the heterointerfaces, we extract the tilt angle ϕ, indicated in Fig. 2(a) from the HRTEM images. Since the STO substrate imposes an isotropic biaxial epitaxial strain on the SL, the in-plane distances along the [100] and [010] directions and the octahedral tilts along those directions are equivalent $\alpha = \beta$ [12]. The angle ϕ is then related to those Glazer angles, or alternatively to the out-of-plane B–O–B bond angle θ_{001} as follows [11]:

$$\theta_{001} = 180° - 2\sqrt{2\,\alpha^2} = 180° - 2\phi \qquad (2)$$

Figures 3(a) and 3(b) show the variation of the measured ϕ angles as a function of adjacent unit cells along $[110]_{pc}$. We use the ϕ values of the bulk materials as references ($\phi_{\text{bulk,STO}} = 0°$, $\phi_{\text{bulk,LNO}} = 7.4°$, $\phi_{\text{bulk,LGO}} = 8.8°$). For both SLs, the tilt angles show similar tendencies. At the substrate–SL interface, the ϕ angles in the first LNO layers gradually change from almost zero towards the bulk LNO value [34]. This can be explained by the adaptation of the structure of the first LNO sublayer of the SL with the one of STO. The cubic STO has no octahedral rotations and when LNO grows epitaxially on it, it has to maintain the octahedral connectivity across the interface. This results in significantly suppressed rotations about the [100] and [010] axes of the NiO$_6$ octahedra in the first LNO sublayer, in agreement with previous observations [35]. The changes in the octahedral tilt patterns caused by the interface with the substrate are confined to the first LNO sublayer of the SLs, in agreement with the results of crystal truncation rod studies performed for LNO ultrathin films grown on STO substrates [36,37]. Further away from the substrate, starting at the first LGO sublayer, the ϕ angle

TABLE I. Mean values for LNO extracted from the TEM measurements for the cation distances $\overline{d}_{001}$ and bond angles $\overline{\theta}_{001}$ along the direction of growth of the SLs. For comparison, the same quantities are provided for a LNO film on STO (* data from Ref. [18]) and bulk LNO (** data from Ref. [5]).

Structure	$\overline{d}_{001}$ (Å)	$\overline{\theta}_{001}$ (deg)
8/4	3.86 ± 0.02	165.3 ± 1.6
4/4	3.83 ± 0.02	165.3 ± 1.8
4/8	3.82 ± 0.02	169.6 ± 1.6
LNO on STO*	3.807	159.9 ± 0.6
LNO bulk**	3.838	165.3

oscillates along the growth direction with the period of the bilayer in both SLs. For the 8/4 SL, the oscillation occurs around the ϕ values of the bulk LNO and LGO. For the 4/8 SL, the ϕ values of the LGO sublayers are close to their bulk ϕ, but the LNO sublayers show clearly smaller ϕ values than the bulk LNO.

Figures 3(c) and 3(d) show the d_{001} and d_{100} distances as functions of location in the SLs. We observe that the in-plane lattice parameter for both SLs is equal to the STO substrate lattice constant within the error bars. This indicates full epitaxial growth of both SLs on STO with the same in-plane lattice parameter. In contrast, the out-of-plane lattice parameter, which can freely adapt, shows a stronger dependency on the SL stacking sequence. In both SLs, the out-of-plane lattice parameter oscillates along the growth direction with the bilayer period, but the magnitude of the oscillation is different. In both samples, the LGO out-of-plane distances are around the values of bulk LGO, while the LNO has significantly different values in the two SLs. In the substrate region of the 8/4 SL, a 1% lattice expansion was found in the first LNO sublayer, in agreement with previous studies on LNO-STO interfaces [38]. Farther from the substrate, the out-of-plane lattice parameter oscillates gradually between the bulk LNO and LGO values with the period of the bilayer. In the 4/8 sample, out-of-plane distances also oscillate with the bilayer period, however, the variation within the LNO sublayers is much stronger, showing a significant out-of-plane lattice compression in the inner two unit cells of the LNO layers. The d values here are as low as 3.8 Å and in good agreement with the c-axis parameters of LNO films grown on STO [18].

Overall, the data in Fig. 3 show that the evolution of the octahedral rotations across the LNO-LGO interfaces is smoother for the 8/4 than for the 4/8 variant. At related SrRuO$_3$ heterointerfaces, a thickness-dependent structural phase transition was explained by relaxation of the octahedral tilts in fully strained films [39], which can be engineered by layer-by-layer control of buffer layers at the heterointerface [14]. In Table I, we summarize the average out-of-plane lattice parameter $\overline{d}_{001}$ and bond angle $\overline{\theta}_{001}$ of the stabilized LNO and LGO structures in n/m SLs. For comparison, we reevaluated data from earlier experiments on a 4/4 LNO-LGO SL grown epitaxially on (001) STO substrate [17] (details are given in the Appendix). While the mean $\overline{d}_{001}$ of the 4/8 and 4/4 SLs are similar and significantly smaller than for the bulk LNO, the $\overline{\theta}_{001}$ angles of the 8/4 and 4/4 SLs are the same and
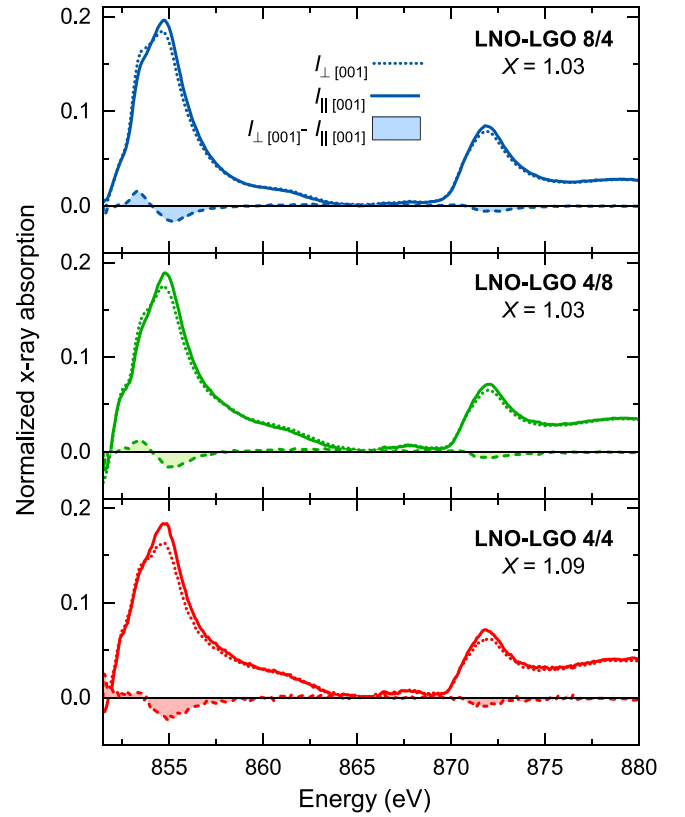

FIG. 4. X-ray absorption linear dichroism measured with linearly polarized light in-plane ($\perp$ [001]) and out-of-plane ($\parallel$ [001]) on LNO-LGO SLs with different stacking sequence 8/4 (top panel, blue lines), 8/4 (middle panel, green lines), and 4/4 (bottom panel, red lines). The dichroic difference spectrum (shown at the bottom of each panel) is characterized by a net integral. Using the sum rule for linear dichroism [Eq. (3)] we determined the e_g hole ratio by integrating the spectra ($I_{\perp[001]}$, $I_{\parallel[001]}$) in the energy from 852 to 875 eV. The results for X are stated in each panel.

bulklike. In contrast, for the 4/8 SL we find a straightening of the octahedra compared to the bulk.

Extracting d_{001} and θ_{001} with unit-cell resolution, we find that two regions within the LNO sublayers can be distinguished in each sample, and we obtain different lattice parameters d_{001} and bond angles θ_{001} for the central (C) and interface (IF) unit cell layers [Figs. 5(a) and 5(b)]. Note that we excluded the first LNO sublayer next to the STO substrate from this evaluation.

To gain information about the relationship between the structural reconstructions and modifications of the electronic structure, we measured x-ray absorption at the Ni-$L_{3,2}$ edges for all three SLs. In particular, we measured the spectra with in-plane $I(E)_{\perp[001]}$ and out-of-plane $I(E)_{\parallel[001]}$ polarization of the incoming x rays. The quantitative information was obtained by applying the sum rules for linear dichroism [19], which provides the ratio X of e_g-orbital holes by

$$X = \frac{h_{3z^2-\mathbf{r}^2}}{h_{x^2-y^2}} = \frac{3I_{\parallel[001]}}{4I_{\perp[001]} - I_{\parallel[001]}}, \tag{3}$$

where $I_{\parallel[001]}$ ($I_{\perp[001]}$) are the energy-integrated intensities across the entire Ni-L edge for $\parallel$ [001] ($\perp$ [001]) polariza-
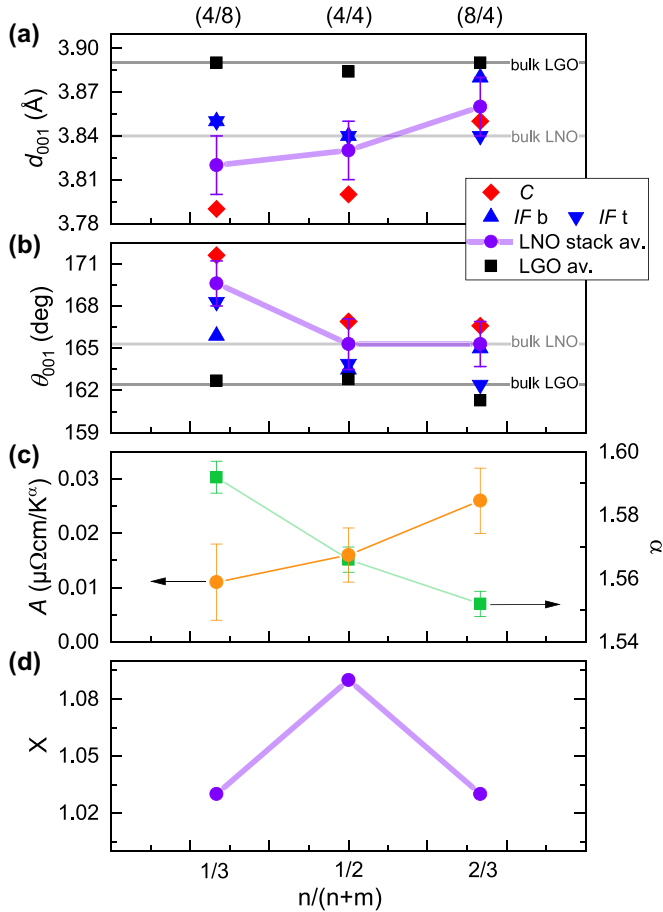
FIG. 5. Relative thickness dependence of LNO and LGO slabs in the different (n/m) SLs parameterized by $n/(n + m)$ as a function of (a) the out-of-plane lattice constant d_{001} and (b) the Ni–O–Ni bond angle θ_{001} in the respective central (C: red diamonds) and interface (IF: blue triangles) layers. In the case of the 8/4 SL, the bottom [IF b: up triangles] and top (IF t: down triangles) interface layers exhibit different θ_{001}. (c) Parameters extracted from fit of $\rho(T)$ shown in Fig. 1. Left: Electron scattering strength coefficient A. Right: Temperature exponent α. (d) Layer-averaged LNO-e_g hole ratio X, obtained from the sum rule analysis of XAS spectra shown in Fig. 4.

tion. The results for X are shown in each panel of Fig. 4. The symmetric 4/4 SL shows the largest orbital polarization with $X = 1.09$ (corresponding to 14% higher $x^2 - y^2$ orbital occupation [19]), whereas the asymmetric 4/8 and 8/4 SLs have lower and equal values of X.

IV. DISCUSSION

We compare all our results in Fig. 5 as a function of relative stacking n/m parameterized by the bilayer fraction $n/(n + m)$ of the LNO layer thickness. We attribute the different structures of the LNO layers in the three SL geometries to the variation in absolute and relative layer thicknesses of the LNO and LGO layers. All SLs were grown on STO substrates with a moderate but different lattice mismatch for LNO and LGO. As discussed in the Introduction, due to their different bulk crystal structures, LNO and LGO are likely to have a different tendency to develop specific octahedral tilts to accommodate

the biaxial strain. The epitaxy in the superlattice and the connectivity across the interfaces results in a compromise structure that depends on the relative layer thicknesses.

The qualitative difference in the tilt patterns of LNO $a^-a^-a^-$ and LGO $a^-a^-c^+$ and the quantitative difference in the strain-stabilized tilt angles determine how the octahedra are connected across the interface. In related (111) NdNiO$_3$ films, this connectivity effect was found to relax at a distance of about $15 - 20$ Å from the interface [7], i.e., the effect is expected to be rather short range in nature compared to the effect of biaxial strain, which is constant over the entire super-lattice to a good approximation. This means that the relative influence of the former potentially varies with the sublayer thickness of $4 - 8$ unit cells ($\sim 15 - 30$ Å) of the SLs studied here.

The set of SLs considered in this paper allows us to par-tially disentangle the effects discussed above. The influence of the LGO sublayer thickness can be seen by comparing the structures of 4/4 and 4/8 SL. In the 4/4 SL, the thinner LNO sublayers are more strongly affected by the interfacial octahedral connectivity constraints, which results in a re-duced out-of-plane lattice parameter and bulklike octahedral rotations [Figs. 5(a) and 5(b)]. An *ab initio* study on LNO films strained to STO showed that a rhombohedrally distorted structure $a^-a^-a^-$ results in higher e_g-orbital polarization (OP) compared to the tetragonally distorted $a^0a^0a^0$ structure [33]. Detailed resonant x-ray reflectometry analysis has shown that the orbital polarization is not uniformly distributed across the 4-u.c.-thick layer sublayers and splits to a lower OP in the two central layers of $X_C = 1.063$ and a higher one in the interface layers of $X_{IF} = 1.117$ of a 4/4 SL [19]. The higher inter-face orbital polarization has been attributed to the effect of electronic confinement resulting from the missing possibility for the 3d electrons to delocalize across the interface to the band-insulating LGO. However, different octahedral distor-tions in the interfacial unit cells [Figs. 3(a) and 3(b)] may have an additional contribution as well. Figure 5 summarizes the structural parameters, out-of-plane lattice spacing d_{001}, and bond angle θ_{001}, and compares them with the coefficient A and exponent α from the fits of $\rho(T)$ [Eq. (1)] shown in Fig. 1, as well as the e_g hole ratio X obtained from XAS. While in the $4/m$ SLs the layer-averaged d_{001} values are comparable, the $n/4$ SLs show similar layer-averaged θ_{001} values [violet points in Figs. 5(a) and 5(b)]. For the 4/4 SL, the pair of values is closest to the bulk values (horizontal gray lines), while the 4/8 has straighter bond angles and smaller d spacing, and the 8/4 has an enlarged d value and bulklike bond angles. Inter-estingly, the 4/4 SL with the smallest deviation of both values compared to bulk shows the highest orbital polarization, that is, the largest hole ratio X [Fig. 5].

The layer-resolved results reveal significant differences for the central (C) [red points in Figs. 5(a) and 5(b)] and interface layers (IF) [blue points in Figs. 5(a) and 5(b)]. The IF d spacing for all SLs is closer to the mean values and bulk LNO, while the d spacing in C layers depends on the LNO slab thickness, i.e., it shows compressed (expanded) values in 4-u.c.-thick (8-u.c.-thick) LNO slabs. The behavior of θ_{001} is similarly complex, but is clearly distinct for the SL with thicker LGO slabs. The thicker the LGO, the larger θ_{001} in C and IF layers. As the bulk value θ_{001} of LGO is smaller
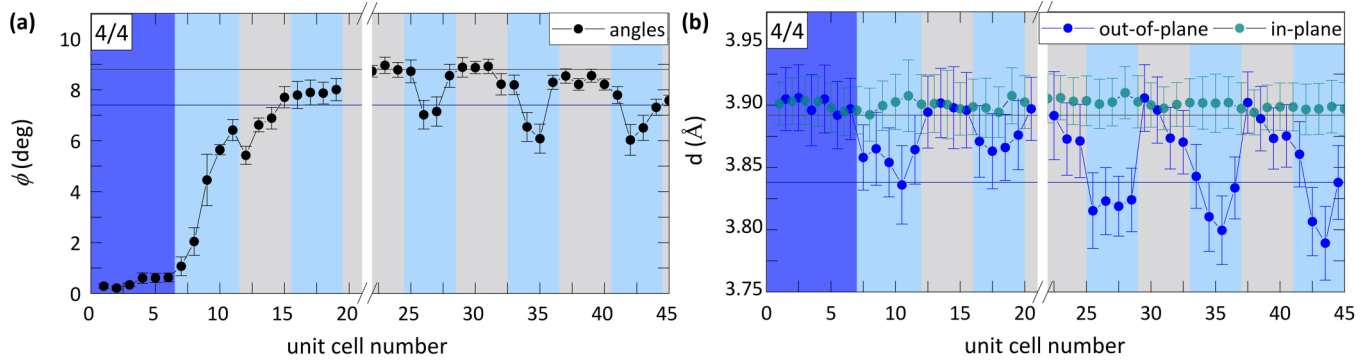
FIG. 6. Quantitative analysis of the 4/4 superlattices on STO substrate. The data were obtained by analyzing the images in Ref. [17] using the CalAtom code [30]. Evaluated values of the (a) ϕ angles (black), (b) out-of-plane (001) (blue) and in-plane (010) (green) lattice spacing as the function of location in the superlattice are shown. Each data point represents the average value of 25 u.c. along the $[1\text{-}10]_{pc}$ direction. The location of the STO substrate (dark blue) and LNO (blue), and LGO (grey) sublayers are marked. The error bars correspond to the standard deviation associated with the statistical averaging. The solid horizontal lines represent the corresponding values of bulk LNO (blue: $\phi_{bulk,LNO} = 7.4°$, $d_{001,bulk,LNO} = 3.838$ Å) and LGO (grey: $\phi_{bulk,LGO} = 8.8°$, $d_{001,bulk,LGO} = 3.892$ Å).

($162.5°$) than the one of LNO ($165°$), this is opposite to the expectations for an imprinted LGO structure. Altogether, we conclude that the d_{001} values depend mainly on the LNO layer thickness, whereas θ_{001} is mainly influenced by the LGO layer thickness.

Interestingly, the resistivity coefficients A and exponents α follow the combined trend of θ_{001} and d_{001}, i.e., they gradually change with the thickness ratio of LNO and LGO layer stacks [Fig. 5(c)]. In previous studies, a correlation between the resistivity exponents and the biaxial strain from the substrate (tensile and compressive strain) and the film thicknesses has been derived [21,24]. Our results show that the detailed structural reconstructions in the form of changes in bond lengths and bond angles, caused by biaxial strain *and* the influence of the second material component in the superlattice, lead to the deviation of the exponent α from Fermi liquid behavior and change the electron scattering strength A. We observe a systematic increase (decrease) of A (α) with increasing SL thickness ratio. The orbital polarization (X) does not simply follow the trend of one or the other, but results from a complex interplay of d_{001} and θ_{001}. To better understand these experimental findings, detailed density functional theory calculations, considering explicitly the different $R\bar{3}c$ and *Pbnm* distortions and the relative thicknesses studied here would be desirable.

V. SUMMARY

We studied the atomic structures stabilized in LNO-LGO n/m superlattices with different relative thickness 4/8, 4/4, and 8/4 all grown on (001) STO substrates. We have shown that the choice of the relative thickness of constituent layers results in different structural distortions under the same conditions of epitaxial strain. We attribute this to the complex interplay of epitaxial strain, the preference of the compounds to form different tilt patterns, and the octahedral connectivity at the interface. The combination of materials that favor a different octahedral tilt pattern leads to a layer thickness dependent accommodation of the epitaxial strain and to different constraints on the octahedral connectivity at the interface. Our

results show that these structural variations are related in a complex way to physical properties such as the resistivity and the orbital polarization of the Ni-d states in the samples. A fundamental understanding of the underlying mechanisms will open up the prospect of the targeted realization of desired structural properties in superlattices and thus the creation of materials with different functionality.

APPENDIX: REEVALUATION OF 4/4 HRTEM DATA

For further comparison, we reproduce the evaluation of our earlier HRTEM investigations on 4/4 LNO-LGO superlattice grown epitaxially on (001) STO substrate (Fig. 6) [17]. To obtain consistent data sets for all SLs, we reevaluated the images of the 4/4 in Ref. [17] also using the CALATOM code [30]. Again, in the vicinity of the cubic STO substrates, the rotations around the in-plane [100] and [010] axes in the first LNO and first LGO sublayers are significantly suppressed. The second LNO sublayer relaxes towards its bulk values. This is in good agreement with the spatial range of substrate-interface coupling observed in the 8/4 and 4/8 samples.

The in-plane lattice parameter along the $[1\text{-}10]_{pc}$ direction [Fig. 6(b)] corresponds to that of the STO substrate and indicates that the same substrate-induced tensile strain acts as in the 8/4 and 4/8 superlattices. The out-of-plane lattice parameter oscillates with the bilayer period along the growth direction. In the vicinity to the substrate, the out-of-plane lattice parameter of the first two LNO sublayers shows a $\sim1\%$ expansion. Within the LNO sublayers, the out-of-plane parameter shows a similar behavior to the 4/8 sample: strong

out-of-plane compression is observed in the inner unit cells, while the LNO unit cells at the interface show higher d_{001} values. The ϕ angle also varies with the period of the bilayer. The ϕ values of the LGO sublayers are close to those of

bulk LGO, while the LNO sublayers show slightly suppressed octahedral rotations around the [100] and [010] axes. The suppression is less pronounced than in the 4/8 sample and more comparable to the ϕ values of the 8/4 sample.

---

[1] J. B. Torrance, P. Lacorre, A. I. Nazzal, E. J. Ansaldo, and C. Niedermayer, Phys. Rev. B **45**, 8209 (1992).

[2] J.-S. Zhou, J. B. Goodenough, B. Dabrowski, P. W. Klamut, and Z. Bukowski, Phys. Rev. Lett. **84**, 526 (2000).

[3] T. Mizokawa, D. I. Khomskii, and G. A. Sawatzky, Phys. Rev. B **61**, 11263 (2000).

[4] R. J. Green, M. W. Haverkort, and G. A. Sawatzky, Phys. Rev. B **94**, 195127 (2016).

[5] J. L. García-Muñoz, J. Rodríguez-Carvajal, P. Lacorre, and J. B. Torrance, Phys. Rev. B **46**, 4414 (1992).

[6] B. Li, D. Louca, S. Yano, L. G. Marshall, J. Zhou, and J. B. Goodenough, Adv. Electron. Mater. **2**, 1500261 (2016).

[7] Y. E. Suyolcu, K. Fürsich, M. Hepting, Z. Zhong, Y. Lu, Y. Wang, G. Christiani, G. Logvenov, P. Hansmann, M. Minola, B. Keimer, P. A. van Aken, and E. Benckiser, Phys. Rev. Mater. **5**, 045001 (2021).

[8] M. Hepting, R. J. Green, Z. Zhong, M. Bluschke, Y. E. Suyolcu, S. Macke, A. Frano, S. Catalano, M. Gibert, R. Sutarto, F. He, G. Cristiani, G. Logvenov, Y. Wang, P. A. van Aken, P. Hansmann, M. Le Tacon, J.-M. Triscone, G. A. Sawatzky, B. Keimer, and E. Benckiser, Nat. Phys. **14**, 1097 (2018).

[9] S. Catalano, M. Gibert, J. Fowlie, J. Íñiguez, J.-M. Triscone, and J. Kreisel, Rep. Prog. Phys. **81**, 046501 (2018).

[10] A. Frano, E. Benckiser, Y. Lu, M. Wu, M. Castro-Colin, M. Reehuis, A. V. Boris, E. Detemple, W. Sigle, P. van Aken, G. Cristiani, G. Logvenov, H.-U. Habermeier, P. Wochner, B. Keimer, and V. Hinkov, Adv. Mater. **26**, 258 (2014).

[11] A. M. Glazer, Acta Crystallogr. Sect. B **28**, 3384 (1972).

[12] J. M. Rondinelli, S. J. May, and J. W. Freeland, MRS Bull. **37**, 261 (2012).

[13] Z. Liao, M. Huijben, Z. Zhong, N. Gauquelin, S. Macke, R. J. Green, S. Van Aert, J. Verbeeck, G. Van Tendeloo, K. Held, G. A. Sawatzky, G. Koster, and G. Rijnders, Nat. Mater. **15**, 425 (2016).

[14] D. Kan, R. Aso, R. Sato, M. Haruta, H. Kurata, and Y. Shimakawa, Nat. Mater. **15**, 432 (2016).

[15] E. J. Moon, R. Colby, Q. Wang, E. Karapetrova, C. M. Schlepütz, M. R. Fitzsimmons, and S. J. May, Nat. Commun. **5**, 5710 (2014).

[16] B. Chen, N. Gauquelin, R. J. Green, J. H. Lee, C. Piamonteze, M. Spreitzer, D. Jannis, J. Verbeeck, M. Bibes, M. Huijben, G. Rijnders, and G. Koster, Nano Lett. **21**, 1295 (2021).

[17] H. Y. Qi, M. K. Kinyanjui, J. Biskupek, D. Geiger, E. Benckiser, H.-U. Habermeier, B. Keimer, and U. Kaiser, J. Mater. Sci. **50**, 5300 (2015).

[18] S. J. May, J.-W. Kim, J. M. Rondinelli, E. Karapetrova, N. A. Spaldin, A. Bhattacharya, and P. J. Ryan, Phys. Rev. B **82**, 014110 (2010).

[19] M. Wu, E. Benckiser, M. W. Haverkort, A. Frano, Y. Lu, U. Nwankwo, S. Brück, P. Audehm, E. Goering, S. Macke, V.

Hinkov, P. Wochner, G. Christiani, S. Heinze, G. Logvenov, H. U. Habermeier, and B. Keimer, Phys. Rev. B **88**, 125124 (2013).

[20] K. A. Borup, K. F. F. Fischer, D. R. Brown, G. J. Snyder, and B. B. Iversen, Phys. Rev. B **92**, 045210 (2015).

[21] J. Fowlie, M. Gibert, G. Tieri, A. Gloter, J. Íñiguez, A. Filippetti, S. Catalano, S. Gariglio, A. Schober, M. Guennou, J. Kreisel, O. Stéphan, and J.-M. Triscone, Adv. Mater. **29**, 1605197 (2017).

[22] F. Wrobel, A. F. Mark, G. Christiani, W. Sigle, H.-U. Habermeier, P. A. van Aken, G. Logvenov, B. Keimer, and E. Benckiser, Appl. Phys. Lett. **110**, 041606 (2017).

[23] J. Zhang, H. Zheng, Y. Ren, and J. F. Mitchell, Cryst. Growth Des. **17**, 2730 (2017).

[24] Q. Guo, S. Farokhipoor, C. Magén, F. Rivadulla, and B. Noheda, Nat. Commun. **11**, 2949 (2020).

[25] J. Stöhr and H. Siegmann, *From Fundamentals to Nanoscale Dynamics* (Springer, Berlin, 2006).

[26] L. Lechner, J. Biskupek, and U. Kaiser, Microsc. Microanal. **18**, 379-384 (2012).

[27] W. van Mierlo, D. Geiger, A. Robins, M. Stumpf, M. L. Ray, P. Fischione, and U. Kaiser, Ultramicroscopy **147**, 149 (2014).

[28] M. Lentzen, B. Jahnen, C. Jia, A. Thust, K. Tillmann, and K. Urban, Ultramicroscopy **92**, 233 (2002).

[29] J. W. Freeland, J. Liu, M. Kareev, B. Gray, J. W. Kim, P. Ryan, R. Pentcheva, and J. Chakhalian, Europhys. Lett. **96**, 57004 (2011).

[30] Q. Zhang, L. Zhang, C. Jin, Y. Wang, and F. Lin, Ultramicroscopy **202**, 114 (2019).

[31] L. Vasylechko, A. Matkovskii, D. Savytskii, A. Suchocki, and F. Wallrafen, J. Alloys Compd. **291**, 57 (1999).

[32] J. M. Rondinelli and N. A. Spaldin, Phys. Rev. B **81**, 085109 (2010).

[33] O. E. Peil, M. Ferrero, and A. Georges, Phys. Rev. B **90**, 045128 (2014).

[34] J. Fowlie, C. Lichtensteiger, M. Gibert, H. Meley, P. Willmott, and J.-M. Triscone, Nano Lett. **19**, 4188 (2019).

[35] S. J. May, C. R. Smith, J.-W. Kim, E. Karapetrova, A. Bhattacharya, and P. J. Ryan, Phys. Rev. B **83**, 153411 (2011).

[36] I. Cheng Tung, G. Luo, J. H. Lee, S. H. Chang, J. Moyer, H. Hong, M. J. Bedzyk, H. Zhou, D. Morgan, D. D. Fong, and J. W. Freeland, Phys. Rev. Mater. **1**, 053404 (2017).

[37] M. Anada, K. Kowa, H. Maeda, E. Sakai, M. Kitamura, H. Kumigashira, O. Sakata, Y. Nakanishi-Ohno, M. Okada, T. Kimura, and Y. Wakabayashi, Phys. Rev. B **98**, 014105 (2018).

[38] J. Hwang, J. Y. Zhang, J. Son, and S. Stemmer, Appl. Phys. Lett. **100**, 191909 (2012).

[39] R. Aso, D. Kan, Y. Shimakawa, and H. Kurata, Adv. Funct. Mater. **24**, 5177 (2014).